

Article

The Aerosol Index and Land Cover Class Based Atmospheric Correction Aerosol Optical Depth Time Series 1982–2014 for the SMAC Algorithm

Emmihenna Jääskeläinen *, Terhikki Manninen , Johanna Tamminen and Marko Laine 

Finnish Meteorological Institute, Erik Palménin aukio 1, 00560 Helsinki, Finland;
terhikki.manninen@fmi.fi (T.M.); johanna.tamminen@fmi.fi (J.T.); marko.laine@fmi.fi (M.L.)

* Correspondence: emmihenna.jaaskelainen@fmi.fi; Tel.: +358-504-546-836

Received: 2 October 2017; Accepted: 24 October 2017; Published: 27 October 2017

Abstract: Atmospheric effects, especially aerosols, are a significant source of uncertainty for optical remote sensing of surface parameters, such as albedo. Also to achieve a homogeneous surface albedo time series, the atmospheric correction has to be homogeneous. However, a global homogeneous aerosol optical depth (AOD) time series covering several decades did not previously exist. Therefore, we have constructed an AOD time series 1982–2014 using aerosol index (AI) data from the satellite measurements of the Total Ozone Mapping Spectrometer (TOMS) and the Ozone Monitoring Instrument (OMI), together with the Solar zenith angle and land use classification data. It is used as input for the Simplified Method for Atmospheric Correction (SMAC) algorithm when processing the surface albedo time series CLARA-A2 SAL (the Surface ALbedo from the Satellite Application Facility on Climate Monitoring project cLoud, Albedo and RADIation data record, the second release). The surface reflectance simulations using the SMAC algorithm for different sets of satellite-based AOD data show that the aerosol-effect correction using the constructed TOMS/OMI based AOD data is comparable to using other satellite-based AOD data available for a shorter time range. Moreover, using the constructed TOMS/OMI based AOD as input for the atmospheric correction typically produces surface reflectance values closer to those obtained using in situ AOD values than when using other satellite-based AOD data.

Keywords: aerosols; aerosol index; SMAC; atmospheric correction; surface reflectance

1. Introduction

The surface albedo, defined as the fraction of incoming radiation reflected hemispherically by the surface, is an essential climate variable (ECV) and directly related to the surface radiation budget [1]. The changes in the surface albedo over a longer period indicate, for example, the impact that climate change has over the Arctic [2]. Since the surface albedo is observed in optical wavelengths, atmospheric effects—especially aerosols—are a significant source of uncertainty. To achieve a homogeneous time series of surface albedo, the atmospheric correction also needs to be homogeneous. However, no global homogeneous aerosol optical depth time series covering several decades previously existed. Some attempts to construct the AOD information in the UltraViolet (UV) range from aerosol index (AI) data have been made [3,4], but there are no daily AOD data in the visible channel for the whole needed time period. The only aerosol—dependent quantity available for the required period is AI, from which we constructed a global daily AOD time series for the atmospheric correction of the surface albedo product in the Satellite Application Facility on Climate Monitoring project (CM SAF), financially supported by European Organisation for the Exploitation of Meteorological Satellites (EUMETSAT). The 34-year long (1982–2015) broadband albedo time series CLARA-A2 SAL (the Surface ALbedo from the CM SAF cLoud, Albedo and RADIation data record, the second version) was produced from Advanced Very

High Resolution Radiometer (AVHRR) measurements [5,6]. The CLARA-A2 SAL algorithm uses the Simplified Method for Atmospheric Correction algorithm (SMAC) [7] for correcting for atmospheric effects. The constructed AOD time series [8] studied in this article was applied to the SMAC algorithm as the aerosol input information.

The AOD-related time series for the visible channel presented here is based on linear regression of the AI at the UV wavelength range from the satellite measurements of the Total Ozone Mapping Spectrometer (TOMS) and the Ozone Monitoring Instrument (OMI), and Solar Zenith Angle (SZA) data with land use classification information [8]. Seasonal effects were paid special attention to, when searching for the relationship of AI and AOD. The AOD time series is constructed specifically for the needs of atmospheric correction, such as needed for generation of the CLARA-A2 SAL data record. In addition, the emphasis of our AOD data set is in the range 0 ... 1 because AOD values larger than that are not accepted for SAL processing. It is challenging to try to estimate the surface parameters accurately in cases with AOD exceeding unity.

The main objective of this paper is to show that aerosol information based on the statistical relationship between AI and AOD is consistent with other satellite-based and in situ AOD data. More importantly, the atmospheric correction based on the constructed AOD data should be close to the results produced applying the SMAC algorithm to other satellite-based or in situ AOD values. In this study, the AI data are used as a proxy for the total column AOD everywhere, even though AI is only largely sensitive to smoke, desert dust and volcanic ash [9]. This is a conscious choice due to lack of any other applicable data for the whole needed period 1982–2014.

This paper is organized as follows. In Section 2, we describe the data used in the comparisons of diverse AOD values and their effect on the atmospheric correction when using the SMAC algorithm. The comparisons between constructed AOD data and the other AOD data are shown in Section 3. The effect of the diverse AOD data sets on the atmospheric correction is studied in Section 4.

2. Data

The data used in this study are described in Table 1.

2.1. Land Cover Classification Data

The AVHRR Land Use Classification (LUC) data [10] was generated in 1998 using AVHRR imagery acquired between 1981 and 1994. In this study, data with spatial resolution of 1° is used for the subclass division. The 11 classes of the LUC data are divided manually into 65 subclasses based on how close the pixels are located to each other [8]. These subclasses are used to provide possibilities for regional inspection, especially when AOD values are related to the land cover classes and locations. The AVHRR LUC provides accurate land use classification on land, but it is too coarse in coastal areas (resolution of $1^\circ \times 1^\circ$ compared to the needed and used resolution $0.25^\circ \times 0.25^\circ$). Global Land Cover 2000 (GLC2000) provides data of finer spatial resolution, $0.01^\circ \times 0.01^\circ$ [11]. Using the GLC2000 data, we construct a water mask of $0.25^\circ \times 0.25^\circ$ resolution, where a pixel is marked as water if all the smaller pixels are marked as such. Then, we used the constructed water mask to refine the coastal areas of the AVHRR LUC data.

2.2. AI-Based AOD

We have constructed an AOD-related time series at the wavelength 550 nm (marked as τ_{AI}) for the atmospheric correction process used in generation of the CLARA-A2 SAL data record [8]. It is based on the Level-3 AOD and positive AI data of OMI [12] instrument, and SZA from the years 2005–2008. The AOD and AI data are at first preprocessed, including data screening using MODerate resolution Imaging Spectroradiometer (MODIS) AOD data and estimating the OMI-AOD data at wavelength 550 nm. Then, the AI and AOD data are deseasonalized within each subclass to remove annual variation. After that, the regressions are made pixel-wise by using the function

$$\tilde{\tau}_{AI} = \alpha \cdot AI \cdot \cos(\theta) + \beta, \quad (1)$$

where θ is the SZA. Use of either means or medians for Equation (1) was tested and the best regression functions, derived for each regional subclass out of 65, were chosen.

The τ_{AI} time series is then calculated from the AI values from the Level-3 data of OMI and TOMS instruments (Nimbus-7 and Earth Probe) [13,14] by using the chosen functions. The resolution of the CLARA-A2 SAL product is $0.25^\circ \times 0.25^\circ$ and hence the τ_{AI} time series is constructed in this resolution. In the comparisons with other satellite-based AOD data, the same $0.25^\circ \times 0.25^\circ$ resolution is used by resampling when the resolutions differ. The intended use of the τ_{AI} facilitates its retrieval by three major advantages: (1) the SMAC algorithm is not developed to cope with AOD values larger than unity so that the needed AOD interval is limited to 0...1, (2) the CLARA-A2 SAL algorithm uses only pixels for which SZA is smaller than 70° , and (3) the atmospheric correction is not executed over water, because the ocean albedo retrieval of CLARA-A2 SAL does not currently use reflectance data at all. The details of the method and time series calculation are described in [8].

2.3. Other Satellite-Based AOD Data

In order to test the quality of the τ_{AI} data, it was compared to three satellite-based AOD data sets: MODIS, Sea-Viewing Wide Field-of-view Sensor (SeaWiFS) and Multi-angle Imaging SpectroRadiometer (MISR) (Table 1). Both the Terra and Aqua satellites carrying the MODIS instrument are used for retrieval of AOD. Terra is on a descending orbit (southward) over the equator and the AOD retrievals are made around 10:30 a.m. local time sun time, and Aqua is on an ascending orbit (northward) over the equator and the AOD retrievals are made around 1:30 p.m. local solar time [15]. The MODIS-AOD data from Aqua Collection 006 are used for this study (marked as τ_{MODIS}) because the timing matches better that of OMI and TOMS. The used AOD data (MYD08) [16] are Level-3 data from Dark Target [17–20] and Deep Blue [21,22] algorithms. The MISR instrument is also aboard the Terra satellite and it has been observing AOD since February 2000. The Level-3 AOD data (MIL3DAE) [23] are used for this study (marked as τ_{MISR}).

The SeaWiFS instrument [24] was launched on August 1997 aboard GeoEye's OrbView-2 (SeaStar) satellite and it started delivering data in September 1997. Due to mechanical failure, SeaWiFS stopped collecting data in December 2010. The AOD data from the SeaWiFS Level-3 data (SWDB_L305) [25] from the Deep Blue algorithm are used for this study (marked as $\tau_{SeaWiFS}$).

2.4. In Situ Data

Aerosol RObotic NETwork (AERONET, [26,27]) provides globally distributed in situ observations of spectral AOD with three data quality levels: Level 1.0 (unscreened), Level 1.5 (cloud-screened) and Level 2.0 (cloud-screened and quality-screened). In this study, we used version 3 Level 1.5 data (daily mean values) because the Level 2.0 data were unavailable. Instead of directly comparing large data pixels ($0.25^\circ \times 0.25^\circ$) with in situ measurements covering tiny areas, we used a window of several pixels against several stations' measurements within the window. These areas are shown in Figure 1. The chosen stations with additional information are listed in Table 2. The AOD at wavelength 550 nm are not measured directly, so that value is calculated using the measured AOD values at wavelengths 440 nm and 675 nm together with the Ångström exponent calculated using AOD values at the same wavelengths (details in [8]). The AOD value for each window is the mean value of these calculated AOD values from each station inside the window (τ_{AER} from now on). The stations used in this study were chosen at various locations around the world and have data for at least five years.

Even though the inspection windows are located all around the globe, they do not cover all diverse aerosol scenarios. However, they offer enough variability to assess the usability of the constructed AOD time series. In window W_2 , located in the Amazon, the AOD values vary a lot; whereas in windows W_1 and W_3 (located on the eastern coast of North America, and in Europe, respectively),

the AOD values are much smaller and vary less. In window W_4 , located over the Sahel, the aerosols are mostly dust from the Sahara, and in inspection window W_5 , the aerosol comes more from urban sources.

Table 1. Summary of the data used in this study.

| | Satellite | Product | Version | Period | L3 Resolution |
|-------------|-----------|--------------------------------------|---------|------------------------------|--------------------------------|
| AOD | | | | | |
| τ_{AI} | - | - | v1.0 | January 1982–December 2014 | $0.25^\circ \times 0.25^\circ$ |
| MISR | Terra | MIL3DAE | V4 | February 2000–December 2014 | $0.50^\circ \times 0.50^\circ$ |
| MODIS | Aqua | MYD08 | 006 | January 2005–December 2014 | $1.00^\circ \times 1.00^\circ$ |
| SeaWiFS | SeaStar | SWDB_L305 | v004 | September 1997–December 2010 | $0.50^\circ \times 0.50^\circ$ |
| AERONET | - | - | v3 | 1999–2014 | - |
| LUC | | | | | |
| AVHRR | - | UMD Global Land Cover Classification | - | 1981–1994 | $1.00^\circ \times 1.00^\circ$ |
| VEGETATION | SPOT 4 | GLC2000 | - | 2000 | $0.01^\circ \times 0.01^\circ$ |

AOD = Aerosol Optical Depth; LUC = Land Use Classification; τ_{AI} = constructed AOD time series; MISR = Multi-angle Imaging SpectroRadiometer; MODIS = MODerate resolution Imaging Spectroradiometer; SeaWiFS = Sea-Viewing Wide Field-of-view Sensor; AERONET = AErosol ROBotic NETwork; AVHRR = Advanced Very High Resolution Radiometer; SPOT = Satellite Pour l’Observation de la Terre; MIL3DAE = MISR Level 3 Component Global Aerosol Product covering a day; MYD08 = MODIS/Aqua Aerosol CloudWater Vapor Ozone Daily L3 Global 1Deg CMG; SWDB_L305 = SeaWiFS Deep Blue Aerosol Optical Depth and Angstrom Exponent Daily Level 3 Data Gridded at 0.5; UMD = University of Maryland, GLC2000 = Global Land Cover 2000.

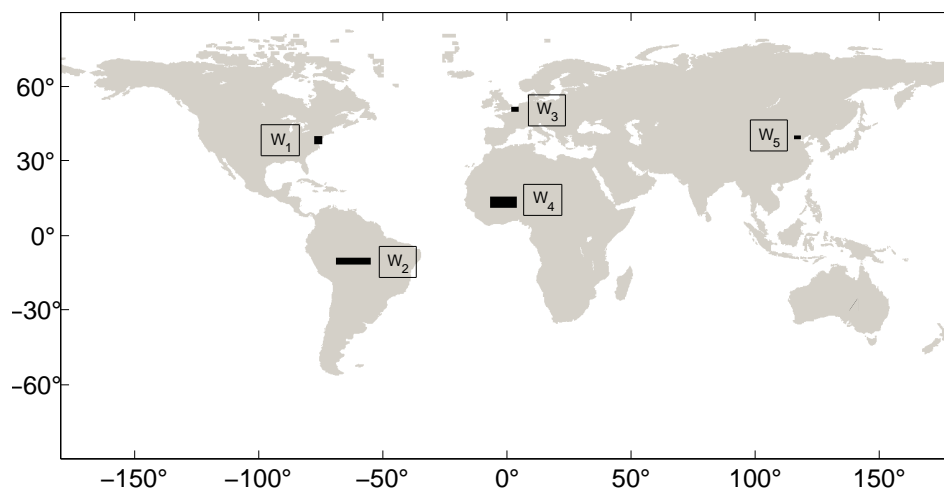


Figure 1. The chosen five inspection windows (W_1 – W_5 black boxes). These contain at least 2 AERONET stations each.

Table 2. Description of the chosen AERONET [27] stations located in each of the inspection window W_1 – W_5 .

| | Name | (Lat, Long) | LUC | Period |
|-------|-------------------|-----------------|---|-----------------|
| W_1 | GSFC | (38.99, -76.83) | wooded grassland | 1999–2014 |
| | MD Science Center | (37.94, -75.48) | mixed coniferous forest and woodland | 1999–2014 |
| | Wallops | (39.28, -76.62) | wooded grassland | 1999–2014 |
| W_2 | Alta Floresta | (-9.87, -56.10) | broadleaf evergreen forest | 1999–2013 |
| | Rio Branco | (-9.96, -67.87) | broadleaf evergreen forest | 2000–2013 |
| W_3 | Dunkerque | (51.04, 2.37) | cultivated crops | 2003–2014 |
| | Lille | (50.61, 3.14) | wooded grassland | 1999–2014 |
| | Oostende | (51.23, 2.93) | cultivated crops | 2001–2014 |
| W_4 | Agoufou | (15.35, -1.48) | grassland | 2002–2011 |
| | Banizoumbou | (13.54, 2.66) | shrubs and bare ground | 1999–2011 |
| | IER Cinzana | (13.28, -5.93) | grassland | 2004–2011 |
| W_5 | Beijing | (39.98, 116.38) | broadleaf deciduous forest and woodland | 2001–2014 |
| | XiangHe | (39.75, 116.96) | broadleaf deciduous forest and woodland | 2001, 2004–2014 |

3. Comparison with In Situ Measurements

The τ_{AI} values are compared to the AERONET AOD data τ_{AER} together with the τ_{MODIS} , $\tau_{SeaWIFS}$ and τ_{MISR} values, to see how well the AOD values from different sources compare. The monthly means for the chosen test windows of τ_{AI} , τ_{AER} , τ_{MODIS} , $\tau_{SeaWIFS}$ and τ_{MISR} are shown in Figure 2. The mean value of the absolute deviations of satellite-based AOD estimates from τ_{AER} are shown in Table 3. In the windows located in North America (W_1), Europe (W_3) and in the Sahel (W_4) (Figure 1), the τ_{AI} data are close to the in situ data and the other satellite-based AOD data. τ_{AI} differs slightly more from τ_{AER} than the other AOD estimates in W_3 and W_4 . The mean difference between the τ_{AER} and τ_{AI} values is zero in the window W_1 , but the other differences are also small in that window. In the window located in the Amazon (W_2), τ_{AI} produces peaks that are clearly too high most of the time compared to the in situ or the other AOD values, but AOD values exceeding unity are in any case too large to be used for atmospheric corrections. In that area, the aerosol index values are similar from year to year, but the AOD values differ more, so the τ_{AI} does not reproduce the AOD values well due to the nature of the time series calculation [8]. The τ_{AI} values differ clearly from the τ_{AER} values compared to the other mean absolute differences. In the window located in China (W_5), all the diverse satellite-based AOD values deviate markedly from the in situ AOD values, except the τ_{MODIS} values. In light of these results, it seems that the Amazon and China areas may cause problems for estimation of the atmospheric correction, whereas areas over Sahara and Sahel, North America and Europe do not.

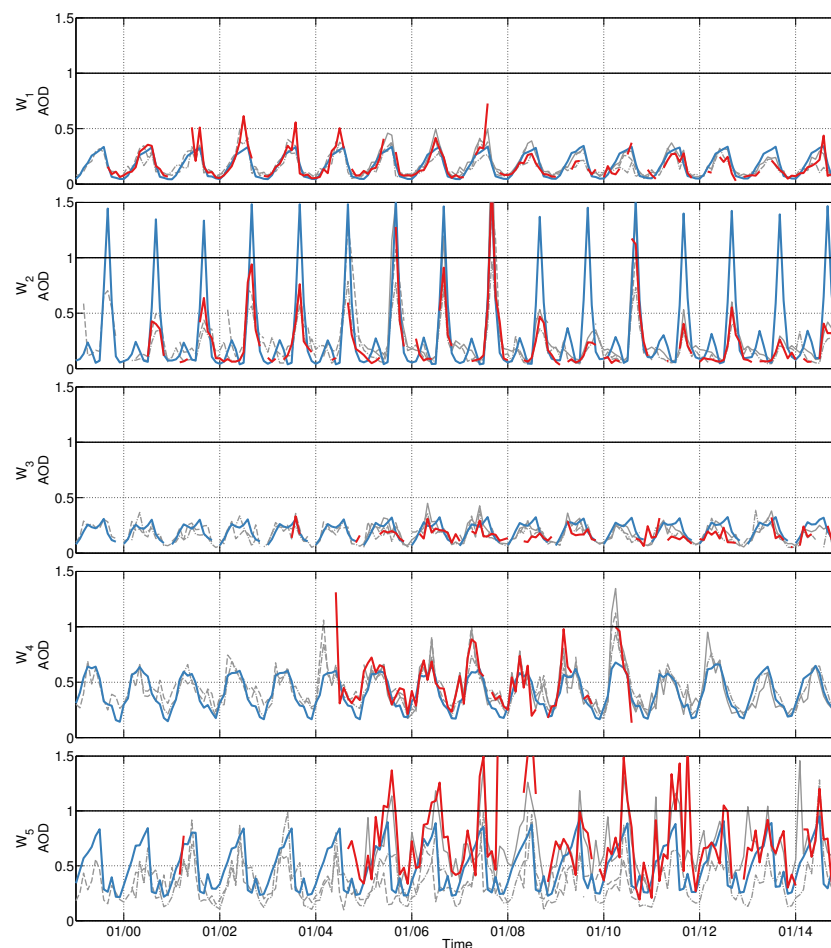


Figure 2. The monthly means of τ_{AI} (blue), τ_{AER} (red), τ_{MODIS} (grey solid line), $\tau_{SeaWIFS}$ (grey dashed line) and τ_{MISR} (grey dash-dot line) in the chosen inspection windows in the years 1999–2014. The black horizontal line indicates the upper limit of the AOD data range usable for the Simplified Method for Atmospheric Correction (SMAC) algorithm.

Table 3. The mean difference between τ_{AER} and the satellite Aerosol Optical Depth (AOD) estimates in the five chosen inspection windows during the time periods presented in Table 2.

| | $\tau_{\text{AI}} - \tau_{\text{AER}}$ | $\tau_{\text{MODIS}} - \tau_{\text{AER}}$ | $\tau_{\text{SeaWIFS}} - \tau_{\text{AER}}$ | $\tau_{\text{MISR}} - \tau_{\text{AER}}$ |
|-------|--|---|---|--|
| W_1 | 0.00 | 0.03 | 0.00 | −0.02 |
| W_2 | 0.15 | 0.06 | 0.06 | −0.02 |
| W_3 | 0.05 | 0.03 | 0.03 | 0.00 |
| W_4 | −0.08 | −0.01 | −0.02 | −0.04 |
| W_5 | −0.22 | −0.06 | −0.39 | −0.35 |

4. The Effect of AOD Estimate on Atmospheric Correction

We performed simulations with the atmospheric correction algorithm SMAC with two wavelength bands, 0.580–0.680 μm (visible, VIS) and 0.725–1.000 μm (Near-infrared, NIR) for the year 2006. The inputs needed for SMAC are the solar zenith and azimuth angle (in degrees), the satellite zenith and azimuth angle (in degrees), water-vapor content (g/cm^2), integrated ozone (atm/cm^2), aerosol optical depth at 550 nm, pressure at surface level (hPa) and top of the atmosphere (TOA) reflectance. The output of SMAC is the surface reflectance (R). For clarification, the notation $R[\tau_{\text{source}}]$ is used in this paper for indicating surface reflectance values calculated by applying the SMAC algorithm to the AOD information from diverse sources (i.e., $R[\tau_{\text{MODIS}}]$ = the surface reflectance values calculated by using τ_{MODIS} as the AOD value). For the simulations, water-vapor content, integrated ozone, surface atmospheric pressure and satellite azimuth angle are set as typical constant values (2.5, 0.35, 1013 and 260, respectively). The sample constant values for the satellite zenith angle are 0° and 40° and for TOA reflectance 0.05, 0.1 and 0.15 for the spectral VIS channel, and 0.2, 0.4 and 0.6 for the spectral NIR channel. Other inputs (AOD, the solar zenith and azimuth angle) vary.

We studied the effect of the τ_{AI} data on the atmospheric correction in two ways. First, we focus on pixel-wise comparisons of surface reflectance values produced using τ_{AI} and the other satellite-based AOD data (MODIS, SeaWIFS and MISR) on five different subclasses (Section 4.1). The chosen subclasses are shown in Figure 3. The subclasses covering the Amazon (subclass 1) and a part of China (subclass 53) were chosen because the τ_{AI} values deviated markedly from τ_{AER} in those areas (Figure 2 and Table 3). The other three subclasses (7, 9 and 39) were chosen mainly because they represent different kinds of aerosols. After the subclass-based study, we focus on the daily mean comparisons of the surface reflectance values calculated using τ_{AER} data of the five windows (Figure 1 and Table 2) and the corresponding τ_{AI} , τ_{MODIS} , τ_{SeaWIFS} and τ_{MISR} data (Section 4.2). The purpose of these studies is to see whether the use of τ_{AI} data as AOD input for the atmospheric correction algorithm produces markedly different results from other satellite-based or in situ AOD values.

4.1. Satellite-Based AOD

We compared the $R[\tau_{\text{AI}}]$, $R[\tau_{\text{SeaWIFS}}]$ and $R[\tau_{\text{MISR}}]$ values to the $R[\tau_{\text{MODIS}}]$ values (monthly means), calculated for the year 2006, for the five chosen subclasses (Figure 3), and the results are shown in Figures 4 (VIS) and 5 (NIR). We also calculated the relative differences of atmospherically corrected surface reflectance values based on all combinations of two different AOD estimates, and the results are shown in Figures 6 (VIS) and 7 (NIR). In these relative difference calculations, the simulated surface reflectance values smaller than 0.01 are omitted. This screening removes approximately 5% of the data from the VIS channel. It does not affect the amounts of data in the NIR channel.

The monthly mean values for the VIS channel in Figure 4 show that the $R[\tau_{\text{AI}}]$ values are consistent with the $R[\tau_{\text{MODIS}}]$ values in the Sahara and quite close in eastern China. In both Siberia subclasses and in the Amazon, the $R[\tau_{\text{AI}}]$ values are slightly smaller than the $R[\tau_{\text{MODIS}}]$ values. The $R[\tau_{\text{SeaWIFS}}]$ and $R[\tau_{\text{MISR}}]$ values are mostly consistent with the $R[\tau_{\text{MODIS}}]$ values in all subclasses; only in Siberia II are there larger outliers.

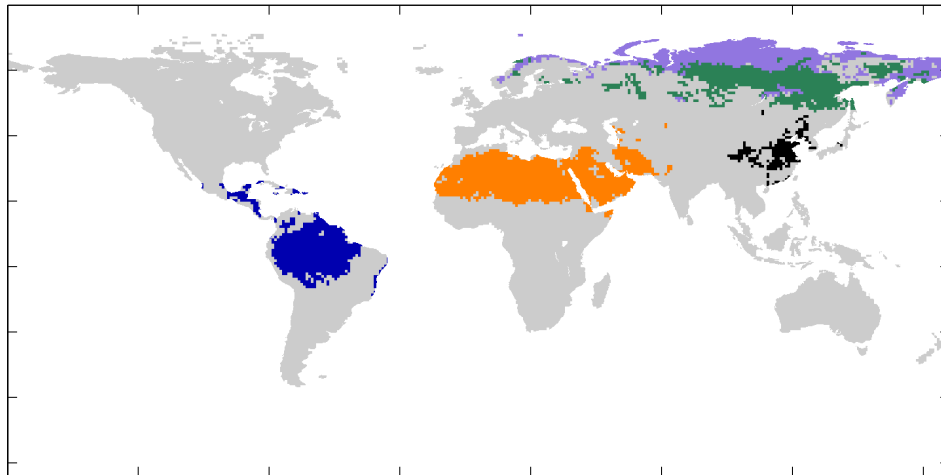


Figure 3. The chosen subclasses for more detailed SMAC simulation inspections: Amazon and surrounds (blue), Sahara and surrounds (orange), Siberia I (green), Siberia II (purple) and part of eastern China (black) [8].

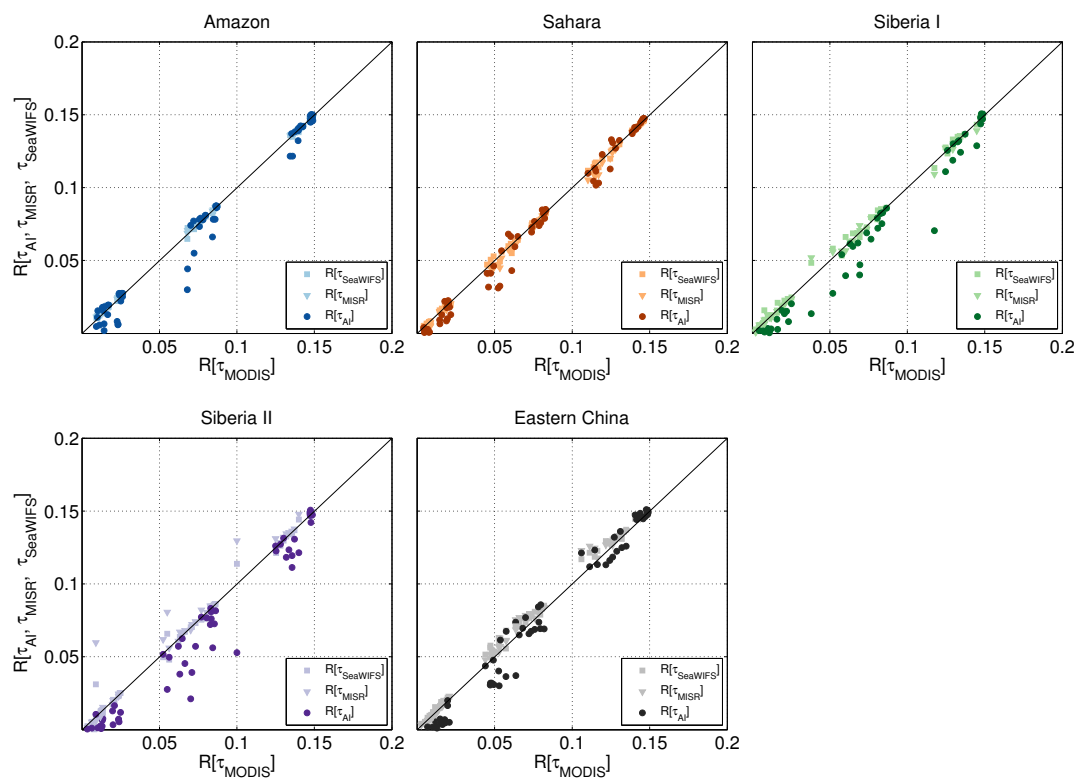


Figure 4. The surface reflectance values simulated by applying the algorithm SMAC in the visible (VIS) channel (0.580–0.680 μm) for Amazon, Sahara, Siberia I, Siberia II and a part of eastern China for each month in the year 2006. The surface reflectance values calculated by using τ_{AI} , τ_{MISR} and τ_{SeaWIFS} as AOD input are compared to those using τ_{MODIS} as AOD input.

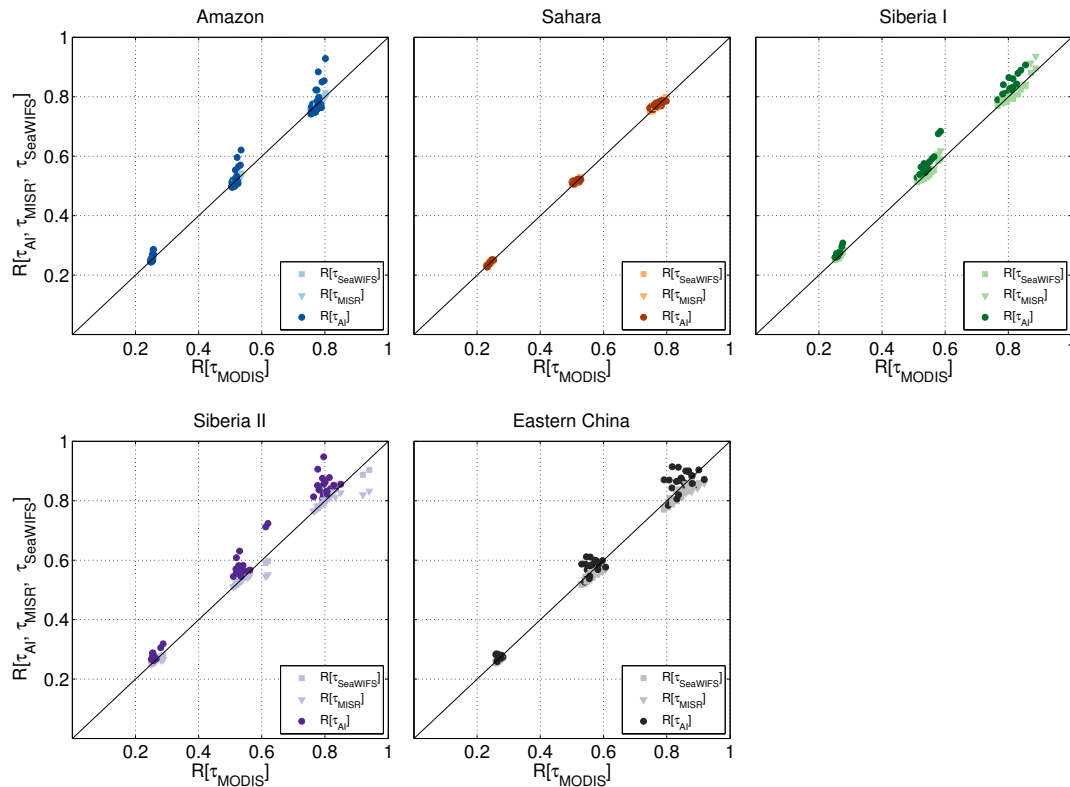


Figure 5. The surface reflectance values simulated by applying the algorithm SMAC in the near-infrared (NIR) wavelength range (0.725–1.000 μm) for Amazon, Sahara, Siberia I, Siberia II and a part of eastern China for each month in the year 2006. The surface reflectance values calculated by using τ_{AI} , τ_{MISR} and $\tau_{SeaWIFS}$ as AOD input are compared to those using τ_{MODIS} as AOD input.

The mutual relative differences for all combinations of two different AOD estimates are shown in Figure 6 for the VIS channel. On average, the relative differences in the subclasses covering the Amazon and the Sahara for all simulated surface reflectance values using different AOD input are close to each other, but there is some seasonal variation. In the Amazon, the most evident difference can be seen in the season September–October–November (SON), where the τ_{AI} corrects the effect of the AOD in the atmosphere from -8 to -5% more than the others. This result is expected due to the overestimation of the τ_{AI} values in September in the Amazon (Figure 2). In the Sahara, a clear difference can be seen in the season March–April–May (MAM), where the τ_{AI} corrects the AOD effect from -14 to -6% more than the others, whereas the other satellite estimates based result are about the same. The subclasses over Siberia I and II are clearly different for τ_{AI} values as AOD input, as the annual $R[\tau_{AI}]$ values are around 10% and 6% higher, respectively, than the other satellite estimates based results. This is due to the large relative differences in the seasons MAM and June–July–August (JJA), the relative difference being -18% at maximum in Siberia I (season JJA), and about -10% in Siberia II (season MAM). The season December–January–February (DJF) is discarded in both subclasses due to the statistically too small number of independent samples, around 2500 values at maximum in Siberia I and about 100 values at maximum in Siberia II, whereas typically the amount of data is from 8000 to over 27 million pixels. Hence, the results from season DJF are ignored. In the eastern China subclass, the $R[\tau_{AI}]$ values compared to the others yield the lowest relative differences on average, but there is also a lot of seasonal variation.

The monthly mean values for the NIR channel show that the $R[\tau_{AI}]$ values are consistent with the $R[\tau_{MODIS}]$ values in the Sahara (Figure 5). In the other subclasses, the $R[\tau_{AI}]$ values tend to exceed the $R[\tau_{MODIS}]$ values. The $R[\tau_{SeaWIFS}]$ and $R[\tau_{MISR}]$ are mostly consistent with the $R[\tau_{MODIS}]$ values in all subclasses.

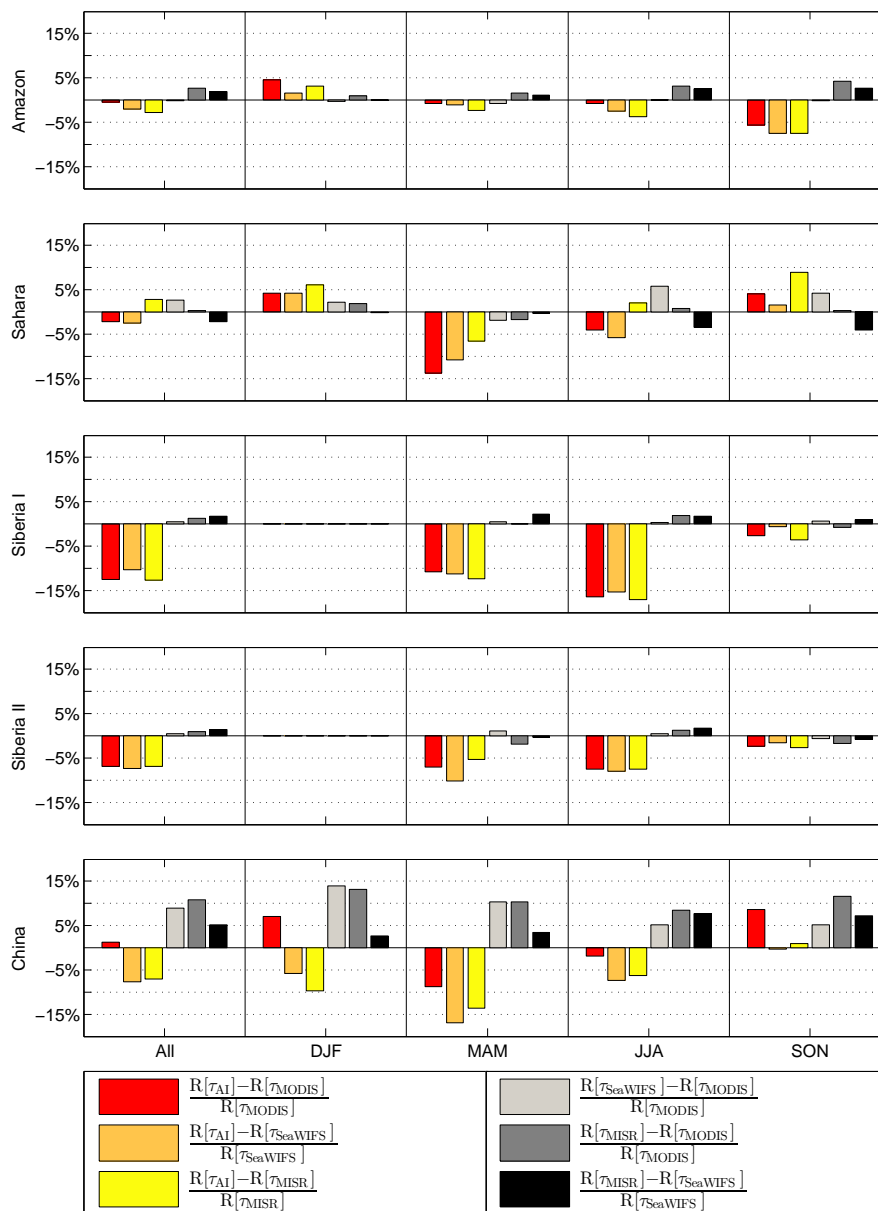


Figure 6. The mean relative differences of the atmospherically corrected surface reflectance values based on all combinations of two different AOD estimates in the VIS channel (0.580–0.680 μm) for the whole year 2006 and three month periods.

The annual relative differences (Figure 7) of NIR channel surface reflectances show that the $R[\tau_{AI}]$ values do not differ much on average from the others in the Amazon. A clear difference can be seen in the seasons JJA and SON, where the $R[\tau_{AI}]$ values differ from 2 to 4% (JJA) and around 5% (SON) from the others, whereas the other relative differences are close to zero in both seasons. In the Sahara, all the relative differences, on average and in all seasons, are small: -1% at minimum and 1% at maximum. Thus, in most cases, the τ_{AI} corrects the aerosol effect as much as the others in the Amazon and in Sahara areas. In both Siberia subclasses, the annual relative differences between the $R[\tau_{AI}]$ values and the others are around 8% in Siberia I and around 4% in Siberia II, whereas the others do not differ from each other in both subclasses. The season DJF is discarded because of statistically too small amount of data, around 5500 values at maximum in Siberia I and around 150 values at maximum in Siberia II, when the amounts are typically 8000 at minimum or over 35 million at maximum. In the seasons MAM and JJA, the $R[\tau_{AI}]$ values differ from 5 to 10% from the others in Siberia I and around

5% in Siberia II, whereas the others do not differ from each other. In the subclass covering eastern China, the annual relative differences between the $R[\tau_{AI}]$ values and the others vary on the average in the range [2%, 5%], whereas the others differ from -3 to -1% from each other. The τ_{AI} corrects the aerosol effect in the atmosphere from 5 to 8% less than the others in the seasons DJF, MAM and JJA.

In general, snow-free land surface reflectance values tend to be higher and the AOD values smaller in the NIR channel [28] (the surface reflectance values varying in the range 0 ... 1) than in the VIS channel (the surface reflectance values varying in the range 0 ... 0.2), and all relative differences in the NIR channel are typically smaller. In the VIS channel, the $R[\tau_{AI}]$ values differ around and over 10% in some areas from the other satellite-based surface reflectance estimates. In the NIR channel, the relative differences are smaller, but there are also areas and seasons for which the $R[\tau_{AI}]$ values differ from the others 10% at maximum.

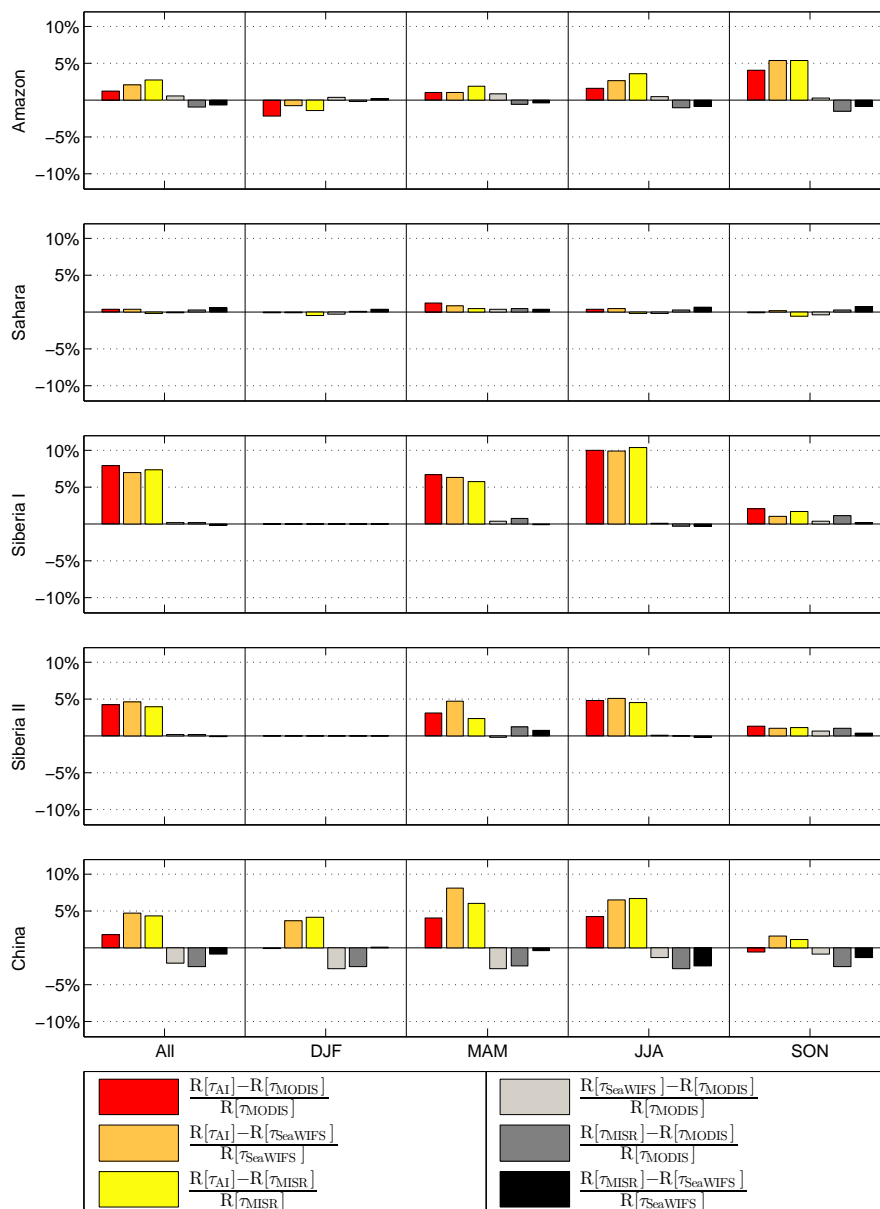


Figure 7. The mean relative differences of the atmospherically corrected surface reflectance values based on all combinations of two different AOD estimates in the NIR channel (0.725–1.000 μm) for the whole year 2006 and three month periods.

4.2. In Situ AOD

We compared the $R[\tau_{AI}]$ values also to the $R[\tau_{AER}]$ values in the five inspection windows (Figure 1 and Table 2), calculated for the year 2006, and the results are shown in Figures 8 (VIS) and 9 (NIR). The monthly mean values for the VIS channel in Figure 8 show that the $R[\tau_{AI}]$ values are consistent with the $R[\tau_{AER}]$ values in the windows W_1 – W_3 . In window W_1 , the $R[\tau_{MODIS}]$ and $R[\tau_{SeaWIFS}]$ values sometimes underestimate the $R[\tau_{AER}]$ values, and in window W_2 the $R[\tau_{SeaWIFS}]$ values overestimates and the $R[\tau_{MODIS}]$ values underestimates. In window W_3 , the $R[\tau_{MISR}]$ and $R[\tau_{SeaWIFS}]$ values are also consistent with the $R[\tau_{AER}]$ values, but the $R[\tau_{MODIS}]$ values underestimates the $R[\tau_{AER}]$ values. In windows W_4 and W_5 , all the satellite-based surface reflectance estimates vary more and in W_5 mostly they overestimate the $R[\tau_{AER}]$ values.

The relative differences for the VIS channel (Figure 10) show that the windows W_1 , W_3 and W_4 are the easiest ones for most satellite-based estimates. In window W_1 , the annual and seasonal relative differences between all the satellite-based surface reflectance estimates and the $R[\tau_{AER}]$ values usually vary from -10 to -5% . The results in window W_3 are similar, but the relative differences are even smaller, except in season SON, for which the $R[\tau_{MODIS}]$ values differ clearly more from the $R[\tau_{AER}]$ values than the others. In window W_4 , all relative differences in seasons DJF, MAM and JJA vary more than the relative differences in windows W_1 and W_3 , but, again in the season SON, the $R[\tau_{MODIS}]$ values differ clearly more from the $R[\tau_{AER}]$ values than the others. The results for the $R[\tau_{AI}]$ values in windows W_1 and W_3 are as expected because, in those areas, aerosol are mainly dust particles and the AOD values are small. This is also what the results of Figure 2 and Table 3 (Section 3) indicated. Windows W_2 and W_5 are clearly more challenging for the satellite-based estimates. In window W_2 in the season MAM, the relative differences are small and have roughly the same magnitude, but, in the season SON, the relative differences vary more, the $R[\tau_{AI}]$ and $R[\tau_{MISR}]$ deviating most from the $R[\tau_{AER}]$. However, in the season JJA, the $R[\tau_{AI}]$ is the closest to the $R[\tau_{AER}]$ values. The season DJF is discarded because of statistically too small amount of data, around six values at maximum, when the typical amount varies in the range 10 ... 290. The comparisons between $R[\tau_{AI}]$ and $R[\tau_{AER}]$ values for window W_2 are better than expected (Table 3, Figure 2). In window W_5 , all the relative AOD differences are large compared to the other windows, but there the annual average of the $R[\tau_{AI}]$ is closest to the $R[\tau_{AER}]$ values.

The monthly mean values for the NIR channel in Figure 9 show that all satellite-based surface reflectance estimates in window W_3 are consistent with the $R[\tau_{AER}]$ values. The $R[\tau_{AI}]$ values are also close to the $R[\tau_{AER}]$ values in windows W_1 and W_2 , whereas other satellite-based surface reflectance estimates deviate more from them. In window W_1 , they are overestimating and in window W_2 they are underestimating the $R[\tau_{AER}]$ values. The $R[\tau_{AI}]$ values vary more in windows W_4 and W_5 than in the other windows, but the same is true for the other satellite-based surface reflectance estimates values. The $R[\tau_{AI}]$, $R[\tau_{MODIS}]$ and $R[\tau_{SeaWIFS}]$ values both under- and overestimates in both windows, and the $R[\tau_{MISR}]$ values underestimates in both windows.

The relative differences for the NIR channel (Figure 11) are small in every inspection window. The relative differences between the $R[\tau_{AER}]$ values and the satellite-based surface reflectance estimates values have roughly the same magnitude in every season in windows W_1 , W_3 and W_4 . There are no data in the season DJF in window W_3 . The results in window W_2 vary more, the $R[\tau_{AI}]$ deviating more from the $R[\tau_{AER}]$ than the other AOD estimates based surface reflectances, but altogether the relative differences are minimal. The season DJF is discarded because of a statistically too small amount of data, around six values at maximum, when the amounts typically vary in the range 10 ... 500. The relative differences in all cases in window W_5 vary more than in the other windows. The $R[\tau_{AI}]$ values either overestimate (MAM and JJA) or underestimate (DJF and SON) the $R[\tau_{AER}]$ values, and the other satellite-based surface reflectance estimates values only underestimate the in situ based surface reflectance values. The annual-mean relative difference from the $R[\tau_{AER}]$ is smallest for the $R[\tau_{AI}]$.

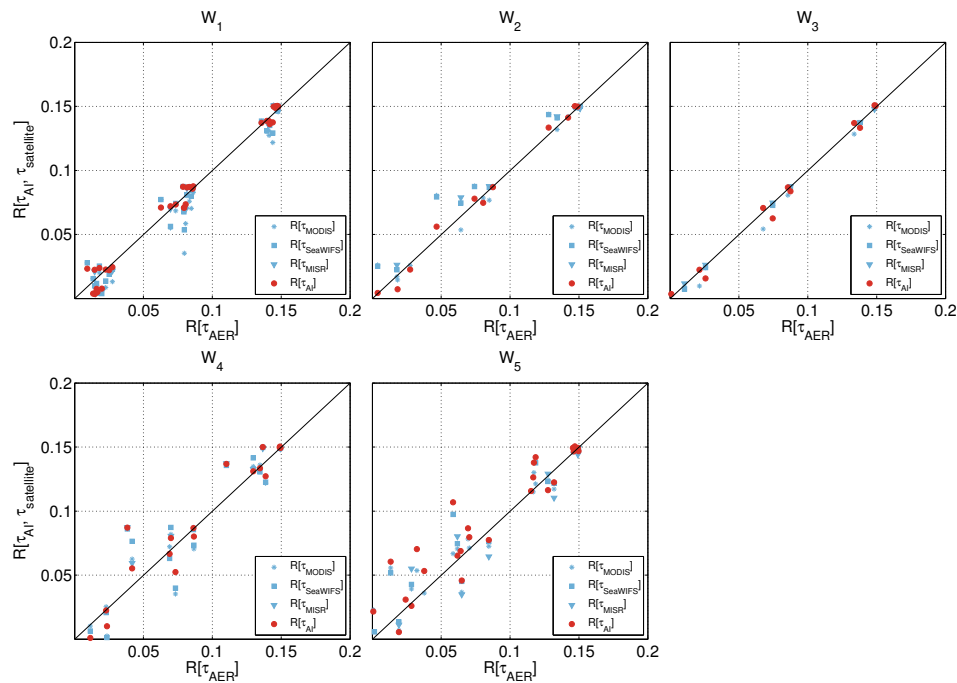


Figure 8. The surface reflectance values R simulated using SMAC in the VIS channel ($0.580\text{--}0.680\ \mu\text{m}$) for the inspection windows $W_1\text{--}W_5$ for each month in the year 2006. The surface reflectance values calculated by using τ_{AI} , τ_{MODIS} , τ_{MISR} and $\tau_{SeaWIFS}$ as AOD input are compared to the $R[\tau_{AER}]$ values.

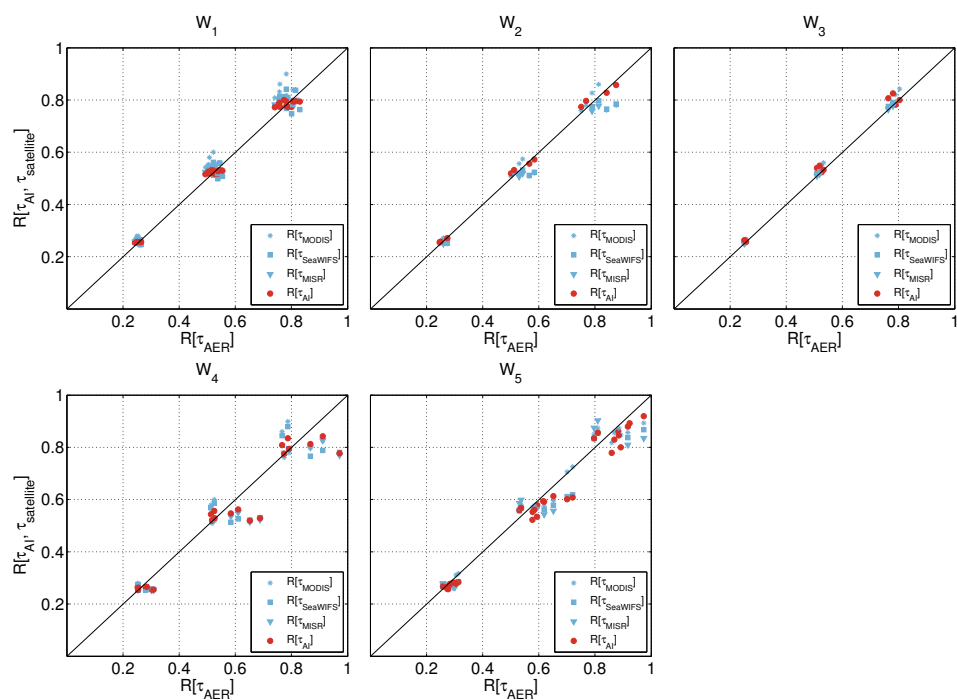


Figure 9. The surface reflectance values R simulated using SMAC in the NIR channel ($0.725\text{--}1.000\ \mu\text{m}$) for the inspection windows $W_1\text{--}W_5$ for each month in the year 2006. The surface reflectance values calculated by using τ_{AI} , τ_{MODIS} , τ_{MISR} and $\tau_{SeaWIFS}$ as AOD input are compared to the $R[\tau_{AER}]$ values.

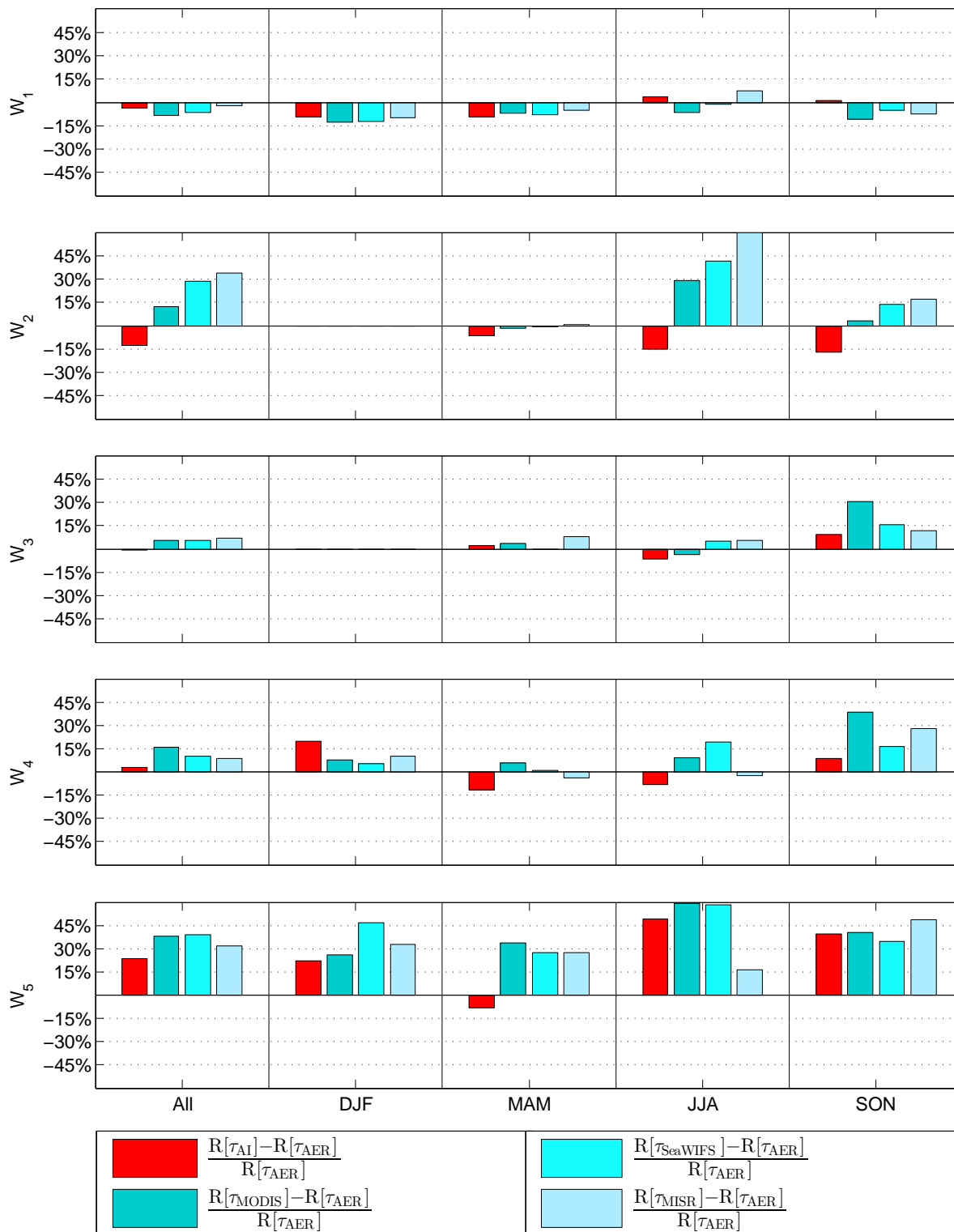


Figure 10. The mean relative differences between between $R[\tau_{AER}]$ and satellite-based surface reflectance estimates in the VIS channel (0.580–0.680 μm) for the whole year 2006 and three month periods.

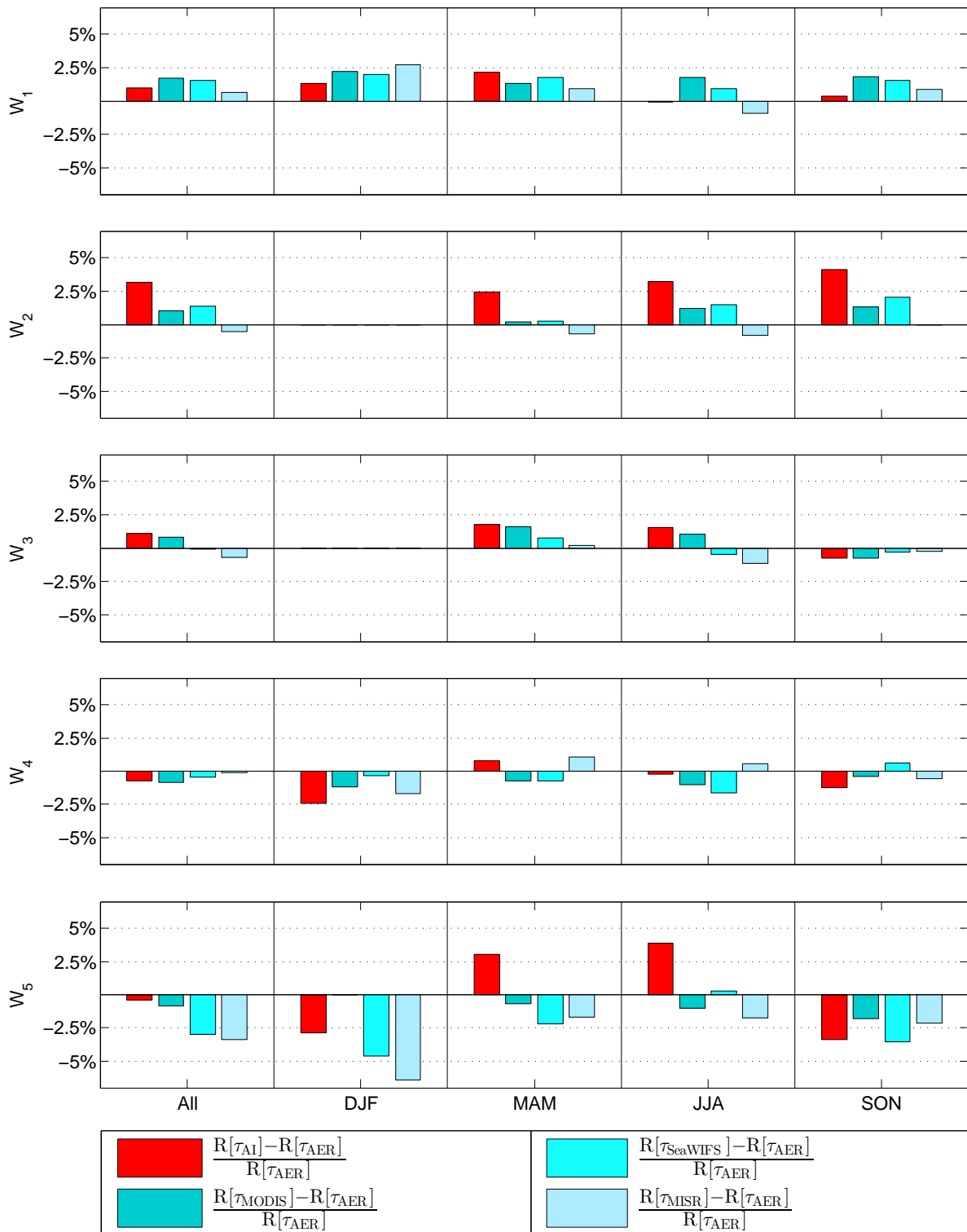


Figure 11. The mean relative differences between between $R[\tau_{AER}]$ and satellite-based surface reflectance estimates in the NIR channel (0.725–1.000 μm) for the whole year 2006 and three month periods.

5. Conclusions

We have constructed an AOD time series 1982–2014 using aerosol index, solar zenith angle and land use classification data. It was used as input for the atmospheric correction algorithm SMAC when processing the surface albedo time series CLARA-A2 SAL. The AOD retrieval algorithm is designed to provide best accuracy at small AOD values (the values varying in the range 0 ... 1) because it is challenging to try to estimate the surface parameters accurately in cases with AOD exceeding unity. We compared the constructed AOD time series to data from both satellite-based and in situ sources in five areas. Best agreement was observed in areas with low AOD levels or mainly dust aerosols. The surface reflectance simulations for one year using different sets of satellite-based AOD data in the VIS and NIR channels show that the atmospheric correction obtained using the constructed AOD data is comparable to that obtained using other satellite-based AOD data. Moreover, using the constructed AOD as input for the atmospheric correction produces typically surface reflectance values closer to those obtained using in situ AOD values for atmospheric correction than when using other satellite-based AOD data for that.

Acknowledgments: This work was financially supported by the EUMETSAT Satellite Application Facility on Climate Monitoring (CM SAF). The work of Johanna Tamminen and Marko Laine was funded by Finnish Academy project INQUIRE. The authors would like to thank the NASA data centers for providing AOD and AI data from the OMI and TOMS instruments, as well as providing AOD data from the MISR, MODIS and SeaWiFS instruments. The authors would like to thank Global Land Cover Facility for providing AVHRR Land Use Classification data and the European Commission Joint Research Centre for providing the GLC2000 Land Use Classification data. The authors want to thank Bernadette Chatenet, Hong-Bin Chen, Herve Delbarre, Philippe Goloub, Brent Holben, Kevin Ruddick, Didier Tarré, Pucai Wang, Xiangao Xia and their staff for establishing and maintaining the 13 sites used in this investigation. The authors want to thank Piet Stammes (KNMI) for his constructive comments. The authors would also like to thank Kaj Andersson (VTT), Aku Riihelä and Niilo Kalakoski (Finnish Meteorological Institute) for helpful discussions.

Author Contributions: Emmihenna Jääskeläinen developed the AOD retrieval method, carried out the validation analysis and wrote the paper. Terhikki Manninen initiated the AOD/AI study, supervised the atmospheric correction related PhD work and contributed to writing the paper. Johanna Tamminen supervised the OMI-related PhD work and contributed to writing. Marko Laine supervised the deseasonalization and statistical analysis and contributed to writing the paper.

Conflicts of Interest: The authors declare no conflict of interest.

Abbreviations

The following abbreviations are used in this manuscript:

| | |
|--------------------|---|
| AOD | Aerosol Optical Depth |
| AI | Aerosol Index |
| SZA | Solar Zenith Angle |
| TOA | Top Of Atmosphere |
| τ_{AI} | constructed AOD time series 1982–2014 |
| τ_{MODIS} | AOD retrieved from MODIS observations |
| τ_{MISR} | AOD retrieved from MISR observations |
| $\tau_{SeaWiFS}$ | AOD retrieved from SeaWiFS observations |
| τ_{AER} | the mean value of calculated AOD values (from AERONET data) at 550 nm |
| τ_{SOURCE} | corresponds to the used AOD information |
| $R[\tau_{SOURCE}]$ | a surface reflectance values calculated using SMAC |
| SMAC | a Simplified Method for Atmospheric Correction algorithm |
| DJF | December–January–February |
| MAM | March–April–May |
| JJA | June–July–August |
| SON | September–October–November |
| CLARA-Ax SAL | the Surface ALbedo from the CMSAF cLoud, ALbedo and RAdition data record, version x |

References

- World Meteorological Organization. The Global Observing System for Climate: Implementation Needs. 2006. Available online: https://library.wmo.int/opac/doc_num.php?explnum_id=3417 (accessed on 2 October 2017).
- Riihelä, A.; Manninen, T.; Laine, V. Observed changes in the albedo of the Arctic sea-ice zone for the period 1982–2009. *Nat. Clim. Chang.* **2013**, *3*, 895–898, doi:10.1038/nclimate1963.
- Hsu, N.C.; Herman, J.R.; Torres, O.; Holben, B.N.; Tanré, D.; Eck, T.F.; Smirnov, A.; Chatenet, B.; Lavenu, F. Comparisons of the TOMS aerosol index with Sun-photometer aerosol optical thickness: Results and applications. *J. Geophys. Res.* **1999**, *104*, 6269–6279, doi:10.1029/1998JD200086.
- Torres, O.; Bhartia, P.K.; Herman, J.R.; Sinyuk, A.; Ginoux, P.; Holben, B. A long-term record of aerosol optical depth from TOMS observations and comparison to AERONET measurements. *J. Atmos. Sci.* **2002**, *59*, 398–413, doi:10.1175/1520-0469(2002)059<0398:ALTROA>2.0.CO;2.
- Karlsson, K.-G.; Anttila, K.; Trentmann, J.; Stengel, M.; Fokke Meirink, J.; Devasthale, A.; Hanschmann, T.; Kothe, S.; Jääskeläinen, E.; Sedlar, J.; et al. CLARA-A2: The second edition of the CM SAF cloud and radiation data record from 34 years of global AVHRR data. *Atmos. Chem. Phys.* **2017**, *17*, 5809–5828, doi:10.5194/acp-17-5809-2017.
- Schulz, J.; Albert, P.; Behr, H.-D.; Caprion, D.; Deneke, H.; Dewitte, S.; Dürr, B.; Fuchs, P.; Gratzki, A.; Hechler, P.; et al. Operational climate monitoring from space: The EUMETSAT Satellite Application Facility on Climate Monitoring (CM-SAF). *Atmos. Chem. Phys.* **2009**, *9*, 1687–1709, doi:10.5194/acp-9-1687-2009. Available online: http://www.cmsaf.eu/EN/Home/home_node.html (accessed on 2 October 2017).
- Rahman, H.; Dedieu, G. SMAC: A simplified method for the atmospheric correction of satellite measurements in the solar spectrum. *Int. J. Remote Sens.* **1994**, *15*, 123–143, doi:10.1080/01431169408954055.
- Jääskeläinen, E.; Manninen, T.; Tamminen, J.; Laine, M. Method for Constructing an AOD Related Atmospheric Correction Time Series for CLARA-A2 SAL Data Record. FMI Reports. 2017. ISBN 978-952-336-013-6 (pdf). Available online: <https://helda.helsinki.fi/handle/10138/224308> (accessed on 2 October 2017).
- Herman, J.R.; Bhartia, P.K.; Torres, O.; Hsu, C.; Seftor, C.; Celarier, E. Global distribution of UV-absorbing aerosols from nimbus-7/TOMS data. *J. Geophys. Res.* **1997**, *102*, 16911–16922, doi:10.1029/96JD03680.
- Hansen, M.; DeFries, R.; Townshend, J.R.G.; Sohlberg, R. UMD Global Land Cover Classification, 1 Degree, 1.0. Department of Geography, University of Maryland, College Park, Maryland, 1981–1994. Available online: <http://glcf.umd.edu/data/landcover/> (accessed on 2 October 2017).
- European Commission Joint Research Centre. The Global Land Cover Map for the Year 2000, 2003. GLC2000 Database. Available online: <http://forobs.jrc.ec.europa.eu/products/glc2000/products.php> (accessed on 2 October 2017).
- Stein-Zweers, D.; Veeffkind, P. OMI/Aura Multi-Wavelength Aerosol Optical Depth and Single Scattering Albedo L3 1 Day Best Pixel in 0.25 Degree × 0.25 Degree V3. 2002. Available online: <http://dx.doi.org/10.5067/Aura/OMI/DATA3004> (accessed on 2 October 2017).
- TOMS Science Team. TOMS/Nimbus-7 Total Ozone Aerosol Index UV-Reflectivity UV-B Erythematol Irradiances Daily L3 Global 1 × 1.25 deg V008. Available online: http://disc.sci.gsfc.nasa.gov/datacollection/TOMSN7L3_V008.html (accessed on 2 October 2017).
- TOMS Science Team. TOMS Earth-Probe Total Ozone (O3) Aerosol Index UV-Reflectivity UV-B Erythematol Irradiance Daily L3 Global 1 deg × 1.25 deg V008. Available online: https://disc.gsfc.nasa.gov/datacollection/TOMSEPL3_008.html (accessed on 2 October 2017).
- Hubanks, P.; Platnick, S.; King, M.; Ridgway, B. MODIS Atmosphere L3 Gridded Product Algorithm Theoretical Basis Document for C6. 2015. Available online: http://modis-atmos.gsfc.nasa.gov/_docs/L3_ATBD_C6.pdf (accessed on 2 October 2017).
- Platnick, S. MODIS Atmosphere L3 Daily Product. 2015. Available online: http://dx.doi.org/10.5067/MODIS/MYD08_D3.006 (accessed on 29 June 2017).
- Kaufman, Y.J.; Tanré, D.; Remer, L.A.; Vermote, E.F.; Chu, A.; Holben, B.N. Operational remote sensing of tropospheric aerosol over land from EOS moderate resolution imaging spectroradiometer. *J. Geophys. Res.* **1997**, *102*, 17051–17067, doi:10.1029/96JD03988.

18. Levy, R.C.; Remer, L.A.; Mattoo, S.; Vermote, E.F.; Kaufman, Y.J. Second-generation operational algorithm: Retrieval of aerosol properties over land from inversion of Moderate Resolution Imaging Spectroradiometer spectral reflectance. *J. Geophys. Res.* **2007**, *112*, doi:10.1029/2006JD007811.
19. Levy, R.C.; Remer, L.A.; Kleidman, R.G.; Mattoo, S.; Ichoku, C.; Kahn, R.; Eck, T.F. Global evaluation of the Collection 5 MODIS dark-target aerosol products over land. *Atmos. Chem. Phys.* **2010**, *10*, 10399–10420, doi:10.5194/acp-10-10399-2010.
20. Remer, L.A.; Kaufman, Y.J.; Tanré, D.; Mattoo, S.; Chu, D.A.; Martins, J.V.; Li, R.R.; Ichoku, C.; Levy, R.C.; Kleidman, R.G.; et al. The MODIS aerosol algorithm, products, and validation. *J. Atmos. Sci.* **2005**, *62*, 947–973, doi:10.1175/JAS3385.1.
21. Hsu, N.C.; Tsay, S.; King, M.D.; Herman, J.R. Aerosol properties over bright-reflecting source regions. *IEEE Trans. Geosci. Remote Sens.* **2004**, *42*, 557–569, doi:10.1109/TGRS.2004.824067.
22. Hsu, N.C.; Jeong, M.-J.; Bettenhausen, C.; Sayer, A.M.; Hansell, R.; Seftor, C.S.; Huang, J.; Tsay, S.C. Enhanced deep blue aerosol retrieval algorithm: The 2nd Generation. *J. Geophys. Res.* **2013**, *118*, 1–20, doi: 10.1002/jgrd.50712.
23. MISR Science Team. Terra/MISR Level 3, Component Global Aerosol Daily, Version 4. 2015. Available online: http://dx.doi.org/10.5067/Terra/MISR/MIL3DAE_L3.004 (accessed on 2 October 2017).
24. Sayer, A.; Hsu, N.C.; Bettenhausen, C.; Jeong, M.J.; Holben, B.N.; Zhang, J. Global and regional evaluation of over-land spectral aerosol optical depth retrievals from SeaWiFS. *Atmos. Meas. Tech.* **2012**, *5*, 1761–1778, doi:10.5194/amt-5-1761-2012.
25. Hsu, N.C.; Sayer, A.M.; Jeong, M.-J.; Bettenhausen, C. SeaWiFS Deep Blue Aerosol Optical Depth and Angstrom Exponent Daily Level 3 Data Gridded at 0.5 Degrees V004. 2013. Available online: <http://dx.doi.org/10.5067/MEASURES/SWDB/DATA301> (accessed on 2 October 2017).
26. Aerosol Robotic Network (AERONET) Homepage. <https://aeronet.gsfc.nasa.gov/> (accessed on 25 October 2017)
27. Holben, B.N.; Eck, T.F.; Slutsker, I.; Tanr, D.; Buis, J.P.; Setzer, A.; Vermote, E.; Reagan, J.A.; Kaufman, Y.J.; Nakajima, T.; et al. AERONET—Federated instrument network and data archive for aerosol characterization. *Remote Sens. Environ.* **1998**, *66*, 1–16, doi:10.1016/S0034-4257(98)00031-5.
28. Clark, R.N.; Swayze, G.A.; Wise, R.; Livo, E.; Hoefen, T.; Kokaly, R.; Sutley, S.J. USGS Digital Spectral Library Splib06a: US Geological Survey. Digital Data Series 231. 2007. Available online: <http://speclab.cr.usgs.gov/spectral.lib06> (accessed on 2 October 2017).



© 2017 by the authors. Licensee MDPI, Basel, Switzerland. This article is an open access article distributed under the terms and conditions of the Creative Commons Attribution (CC BY) license (<http://creativecommons.org/licenses/by/4.0/>).